Available online at www.sciencedirect.com

ScienceDirect

Ceramics International 41 (2015) 13393–13408

CERAMICS INTERNATIONAL

www.elsevier.com/locate/ceramint

The structure and texture genesis of apatite-type lanthanum silicates during their synthesis by co-precipitation

Tamara Kharlamova[a,*], Olga Vodyankina[a], Alexander Matveev[b], Vassilis Stathopoulos[c], Arcady Ishchenko[d,e], Dzhalil Khabibulin[d,e], Vladislav Sadykov[d,e]

[a]Tomsk State University, 36 Lenin Ave., 634050 Tomsk, Russia
[b]Baikal Institute of Nature Management, Siberian Branch of the Russian Academy of Sciences, 6 Sakhyanovoy Str., 670047 Ulan-Ude, Buryatia, Russia
[c]Department of Electrical Engineering, School of Technological Applications, Technological Educational Institute of Sterea Ellada, 34400 Psahna, Greece
[d]Boreskov Institute of Catalysis, Siberian Branch of the Russian Academy of Sciences, 5 Lavrentiev Ave., 630090 Novosibirsk, Russia
[e]Novosibirsk State University, 2 Pirogova Str., 630090 Novosibirsk, Russia

Received 26 June 2015; accepted 21 July 2015
Available online 29 July 2015

Abstract

Peculiarities of genesis of the structure and texture of apatite-type lanthanum silicates, both undoped and doped with aluminum, in the course of co-precipitation followed by sediment thermal treatment were elucidated by using a combination of methods including thermal analysis, XRD, IR spectroscopy, low-temperature adsorption of nitrogen, ^{27}Al and ^{29}Si MAS NMR spectroscopy and TEM with EDX analysis. An amorphous lanthanum silicate with the short-range ordering typical for ortho-diorthosilicate was shown to be formed in the course of precipitation, while its crystallization proceeds via rearrangement of the polymeric structure of primary particles during subsequent thermal treatment.
© 2015 Elsevier Ltd and Techna Group S.r.l. All rights reserved.

Keywords: Apatite; Lanthanum silicate; Co-precipitation; Formation mechanism

1. Introduction

Apatite-type silicates of rare earth elements known for a long time as structural analogs of $Ca_{10}(PO_4)_6F_2$ fluoroapatite [1–7] are considered as promising materials for such applications as matrix for radioactive waste immobilization, lasers and phosphors [2,7–14]. Recently, Peng reported that $La_{9.33}(SiO_4)_6O_2$:Ln^{3+} (Ln=Ce, Eu, Tb) microfibers can provide green and red emission as dependent upon the nature of doping ions, which makes these materials potentially attractive for applications in field emission displays [9]. Li's photoluminescence studies showed that $Ca_{2(1-x)}La_{7.6+x}(SiO_4)_6O_2$:$Eu_{0.4}$-based phosphors could be readily excited by near-UV (387 nm) irradiation, which makes them promising red-emitting materials for commercial near-UV LED-pumped white light emitting diodes, with Li^+ doping resulting in remarkably enhanced photoluminescence performance of these solids [11].

In mid-1990s Nakayama discovered a promising level of oxygen ion conductivity of apatite-type rare earth silicates in the temperature range of 600–700 °C [15,16], and over the past twenty years these materials, particularly lanthanum silicates, have attracted a lot of research interest [17,18]. Numerous studies of structure and transport properties of these compounds demonstrated that their high ion conductivity is associated with the presence of cation vacancies and/or interstitial oxygen atoms in the hexagonal apatite structure, while the structure tolerance to isomorphous substitutions allows to vary the density of defects and, thus, to modify their transport properties [17–27]. Both lanthanum substitution and especially doping on the silicon site with lower valence cations (Ga^{3+}, Al^{3+}, Fe^{3+}) help to increase the oxygen ion conductivity of apatite-type lanthanum silicates making them promising as solid electrolytes for intermediate temperature SOFCs [18,23–26].

*Corresponding author: Tel./fax: +73822200419.
E-mail address: kharlamova83@gmail.com (T. Kharlamova).

http://dx.doi.org/10.1016/j.ceramint.2015.07.128
0272-8842/© 2015 Elsevier Ltd and Techna Group S.r.l. All rights reserved.

Over the recent years apatite-type lanthanum silicates also attracted a lot of interest as catalysts of redox reactions [28–33]. For instance, papers by Nakata group demonstrate that the use of apatite-type lanthanum silicates as a support instead of γ-Al_2O_3 ensures higher catalytic activity of platinum catalysts in NO_x selective reduction by propylene as well as in C_3H_6 oxidation in mixtures containing C_3H_6, NO and O_2 [28–31]. Lanthanum substitution by alkaline and alkali-earth elements was shown to increase activity of such catalysts. Zhang et al. demonstrated a high catalytic activity of $La_{9.33}(SiO_4)_6O_2$ lanthanum silicate with the apatite structure in the oxidative coupling of methane [32]. Isomorphous silicon substitution by aluminum in the apatite structure accompanied by a change in its oxygen stoichiometry was shown to result in significant increase of activity in the oxidative coupling of methane [33].

The conventional method of apatite-type rare-earth silicates preparation is high-temperature solid-phase synthesis [3,5,7,12,14–25]. However, this method does not allow controlling textural characteristics and spatial uniformity of chemical and phase composition of produced silicates playing a crucial role in performance of functional ceramics, phosphor materials as well as bulk or supported catalysts. Increased interest in silicon oxyapatites as solid electrolytes and catalysts stimulated research aimed at developing new methods of their preparation. In particular, a number of low-temperature methods were suggested as alternatives to high-temperature solid-phase synthesis, including methods based on condensation from solutions, namely co-precipitation [34–36], various modifications of sol–gel method [37–45] as well as soft mechanochemical route [46–49]. Some interesting results on preparation of lanthanum silicate by co-precipitation have been published by Li and Yang [34,35]. Thus, Li et al. demonstrated that dispersed powders of undoped lanthanum silicate, which can be sintered into dense (relative density $>95\%$) ceramics at 1300 °C, were successfully produced by co-precipitation [34]. Yang et al. described modified co-precipitation technique to synthesize undoped lanthanum silicates based upon using aqueous ammonia solution with polyethylene glycol (PEG) as dispersant additive, which was believed to prevent particle agglomeration and help to obtain finer powders than in the case of conventional co-precipitation [35]. However, these studies contain rather formal and speculative description of the lanthanum silicates formation, with the main conclusions being made considering characteristics of samples calcined at temperatures above 800 °C [34,35].

In some publications, the effect of synthesis parameters (H_2O/Si ratio, concentration of acid and TEOS, sintering temperature [39]; molar ratio of NO_3^- ions to citric acid and ethylene glycol in the solution [44]; pH of a solution [45]) on the phase composition of undoped apatite-type lanthanum silicate powders produced by precipitate/gel calcination was considered, though genesis of their phase composition, structure and, especially, texture of materials at early stages of synthesis has not been in general studied. Even such studies are scarce in the case of doped apatite-type lanthanum silicates attracting the most interest as solid electrolyte, phosphors, supports and catalysts. Meanwhile, preparation of materials with controlled chemical and phase composition, possessing optimal specific surface area, porous structure and other textural characteristics defined by specific operating conditions requires understanding general physicochemical regularities at each stage of the selected preparation method. Furthermore, precursors (complexes, clusters, intermediate compounds) determining the chemical and phase composition as well as primary particles controlling specific surface and porous structure of products are formed namely at the early stages of synthesis [50–53]. Hence, studies aimed at elucidation of general regularities of lanthanum silicate structure and texture formation are required to ensure tailor-made design of known and new materials (solid electrolytes, laser and phosphor hosts, supports, and catalysts) as well as up-scaling of synthesis process.

In the present paper, peculiarities of genesis of the structure and texture of apatite-type lanthanum silicates, both undoped and doped with aluminum, at early stages of synthesis by co-precipitation were elucidated by using a complex of physicochemical methods, including XRD, IR spectroscopy, thermal analysis, low-temperature adsorption of nitrogen, ^{27}Al and ^{29}Si MAS NMR spectroscopy, and TEM with EDX analysis.

2. Experimental

2.1. Sample preparation

Undoped $La_{10-x}(SiO_4)_6O_{3-3x/2}$ (x=0; 0.67; 0.33) and aluminum-doped $La_{10-y+x/3}(SiO_4)_{6-x}(AlO_4)_xO_{3-3y/2}$ (x=0.25; 0.5; 1; y=0.33; 0.67) samples were produced using techniques described by Li for synthesis of an undoped sample [34]. TEOS (EKOS–1, 99.1%) and water solutions of lanthanum and aluminum nitrates prepared using $La_2(CO_3)_3 \cdot 8H_2O$ (VEKTON, 99.0%) or $La(NO_3)_3 \cdot 6H_2O$ (VEKTON, 99.0%) and $Al(NO_3)_3 \cdot 9H_2O$ (VEKTON, 99.0%), respectively, were used as reagents for lanthanum silicates synthesis. In the case of aluminum-doped samples, at first a stoichiometric amount of aluminum nitrate water solution was added to the prepared lanthanum nitrate solution. Ethanol and TEOS were added to water solution of lanthanum nitrate or a mixed solution of lanthanum and aluminum nitrates. The volume ratio of H_2O: C_2H_5OH was 1:4; lanthanum concentration was 0.4 mol/l. Thus prepared mixed solution was added to aqueous ammonia solution (pH = 9–12) under constant stirring. A white residue was filtered under vacuum, washed three times with distilled water and three times with ethanol, dried at 80 or 120 °C for 12 h, and annealed in the air at different temperatures.

2.2. Methods of sample characterization

Samples were studied by methods of low-temperature adsorption of nitrogen, thermogravimetry (TG) and differential scanning calorimetry (DSC), X-ray phase analysis (XRD), infra-red (IR) spectroscopy and transmission electron microscopy (TEM) with elemental analysis by energy-dispersive X-ray spectroscopy (EDX). Low-temperature adsorption of nitrogen was carried out using specific surface and porosity

analyzer TriStar 3020 ("Micromeritics", USA). Specific surface area was calculated by BET method. To minimize variation of the hydrogel structure under the action of capillary forces, which accompany hydrogel transformation to xerogel, drying was carried out in a rapid mode after changing the water–ethanol mother solution to ethanol.

TG and DSC of xerogel were carried out using NETZSCH STA 449C. Analysis was performed in the flow of O_2/N_2, within the temperature range from 20 to 1000 °C; heating rate was 10 °C/min. Al_2O_3 crucibles were used for analysis.

XRD was performed with XRD-6000 (Shimadzu, Japan) and MiniFlex 600 (Rigaku, Japan) X-ray diffractometers using CuKα radiation (40 kV; 30 and 15 mA, respectively). Scanning was carried out within the angle range of 10–70° (2θ) using scan step of 0.02°. An intrinsic experimental broadening of peaks was estimated using a silicon powder standard. Phase composition of samples was determined using PDF-4 and PCPDFWIN databases, as well as full-profile analysis program POWDER CELL 2.4. The X-ray crystal size D_{XRD} and strain density were calculated using Williamson–Hall method.

IR spectra of samples were registered by IR Fourier spectrometer Nicolet 6700 equipped with Smart Orbit™ diamond ATR accessory (Thermo Scientific, USA) using single-beam optical scheme and built-in Michelson interferometer. Spectra were obtained within the range of 400–4000 cm^{-1} with resolution of 4 cm^{-1}.

TEM studies were performed on a JEM-2010 microscope with EDX Phoenix Spectrometer equipped with Si (Li) detector.

^{27}Al MAS NMR and ^{29}Si MAS NMR data were collected using a Bruker Avance-400 spectrometer operating at 104.2 MHz (ν_r=15 kHz, 25 °C) and 79.4 MHz (ν_r=6 kHz, 25 °C), respectively. WVT-4 MAS probe was used, with the outer diameter of the rotor being 4 mm. ^{29}Si and ^{27}Al chemical shifts are referred to external $SiMe_4$ and $Al(H_2O)_6^{3+}$ standards, respectively.

3. Results

Genesis of the local structure, phase composition and textural characteristics of lanthanum silicate in the course of synthesis was studied for undoped samples with stoichiometry of $La_{10-x}(SiO_4)_6O_{3-3x/2}$, x=0; 0.67; 0.33 and samples doped by aluminum corresponding to a stoichiometry of $La_{10-y+x/3}(SiO_4)_{6-x}(AlO_4)_xO_{3-3y/2}$, x=0.25; 0.5; 1; y=0.33; 0.67.

3.1. Thermal analysis data

Fig. 1 represents typical data of thermal analysis and respective mass-spectrometric (MS) analysis of the gas phase composition for the precipitate dried in air at 120 °C. Gravimetric curves of both unmodified and aluminum-modified samples are similar to the one presented by Li et al. for undoped lanthanum silicate [34] and characterized by the weight loss during heating up to ~800 °C in the air flow, with an essential weight loss occurring in several steps between 25 and 600 °C. According to the MS data, the mass

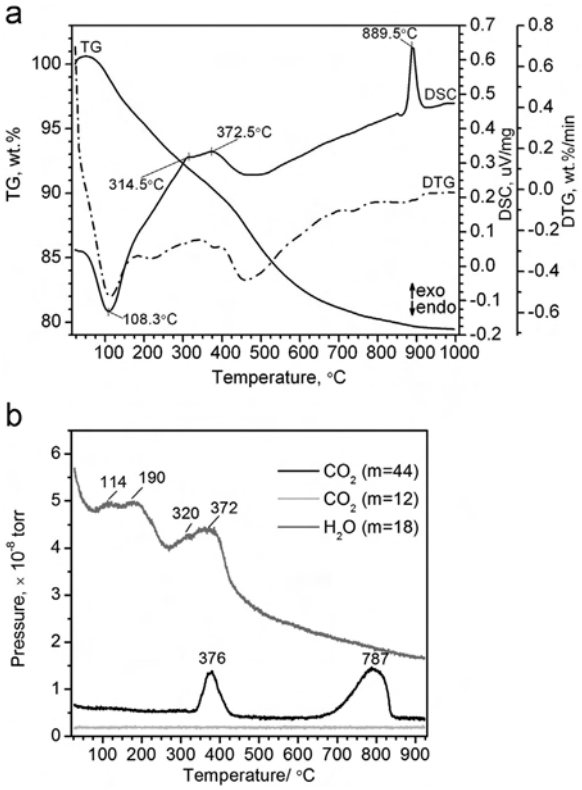

Fig. 1. Typical data of thermal analysis of the precipitate dried in air at 120 °C (a) as well as mass-spectrometric analysis of gas phase during the thermal analysis (b) exemplified by those of the sample corresponding to the stoichiometry of $La_{9.83}(SiO_4)_{5.5}(AlO_4)_{0.5}O_{2.5}$.

change of the sample is caused by removal of water and CO_2 (Fig. 1b). In particular, in the temperature range of 20–325 °C, the mass change is mainly caused by the elimination of water with the maxima at 114, 190 and 320 °C. In the temperature range of 320–450 °C, the mass change is due to both elimination of water (peak with the maximum at 372 °C in the corresponding MS curve) and CO_2 (peak with the maximum at 376 °C in the MS-curve with m=44). In the temperature range of 650–840 °C, the mass change is caused by the continuous water removal accompanied by the CO_2 evolution (peak with maximum at 787 °C in the corresponding MS curve).

The mass change is accompanied by the endothermic effect in the temperature range of 20–160 °C and exothermic effect in the temperature ranges of 160–520 °C and 860–920 °C. According to Li, a broad exothermic peak below 600 °C indicates interaction of $La(OH)_3$ and SiO_2 to form amorphous oxy-apatite phase, while the exothermic effect in the range of 860–920 °C, which is not accompanied by significant change of sample mass, is associated with the phase transition from amorphous to crystalline phase of silicate with the apatite structure [34]. The latter was confirmed by XRD results. However, Li's suggestion on the nature of the exothermic effect below 600 °C, which imply the absence of component interaction during co-precipitation and emergence of primary particles of individual hydroxides/oxides, was not properly justified.

3.2. X-ray diffraction data

The typical X-ray patterns of samples calcined at different temperatures are presented in Fig. 2a. According to XRD data, the precipitate dried at 120 °C is X-ray amorphous (X-ray diffraction pattern is not given for brevity). Precipitate annealing at temperatures below 800 °C does not lead to crystalline phase formation. However, formation of crystalline phase of lanthanum silicate with the apatite structure is observed after sample annealing at 800 °C for 3 h or at 900 °C (Fig. 2a), with X-ray particle sizes D_{XRD} of the crystalline lanthanum silicate estimated from broadening of diffraction peaks amounted to about 27–48 nm (Table 1). Hence, in accordance with the thermal analysis data, XRD data confirm crystallization of lanthanum silicate with the apatite structure above 800 °C. The sample calcination at higher temperatures results in further apatite lattice ordering, X-ray particle size being equal to about 56–81 nm after 1000 °C and 110–134 nm after 1100 °C.

It is noteworthy that some secondary phases can also be formed during sample crystallization depending on sample stoichiometry as well as temperature and duration of its calcinations, which seems to be caused by the components segregation at domain boundaries of the apatite-type lanthanum silicates [21,27,48]. All prepared crystalline samples with the stoichiometry corresponding to the composition within the range of the homogeneous apatite-type phase existence such as $La_{9.33}(SiO_4)_6O_3$, $La_{9.83}(SiO_4)_{5.5}(AlO_4)_{0.5}O_{2.5}$, $La_{9.42}(SiO_4)_{5.75}(AlO_4)_{0.25}O_2$, are single phases (Fig. 2a and b, Table 1). However, La_2O_3 or La_2SiO_5 are present in samples with the stoichiometry corresponding to the composition outside the homogeneity range. Thus, $La_{10}(SiO_4)_6O_3$ sample calcined at 1000 °C or 1100 °C contains some admixture of La_2O_3 or La_2SiO_5 phases, respectively (Fig. 2b, Table 1), which is in agreement with literature data [21,27]. There are traces of La_2O_3 phase in $La_{9.67}(SiO_4)_6O_3$ sample calcined at 1100 °C for 3 h (Table 1), with the sample composition being close to the boundaries of the region of the homogeneous apatite-type phase existence in the La_2O_3–SiO_2 system [21,27]. A prolonged sample calcination at 1100 °C or its calcination at higher temperatures should apparently result in La_2SiO_5 phase formation instead of lanthana [34]. It is interesting that La_2O_3 phase formation precedes appearance of La_2SiO_5 phase during lanthanum silicates crystallization from precipitate, which was also observed by Li [34]. This implies a sequential mechanism of their formation. However, no crystalline phase of a lanthana precursor (lanthanum hydroxide or lanthanum carbonate) has been detected in the sample. This can be explained either by an amorphous state of the lanthana precursor or by a decomposition of nonstoichiometric lanthanum silicate with segregation of the lanthanum excess as La_2O_3 phase.

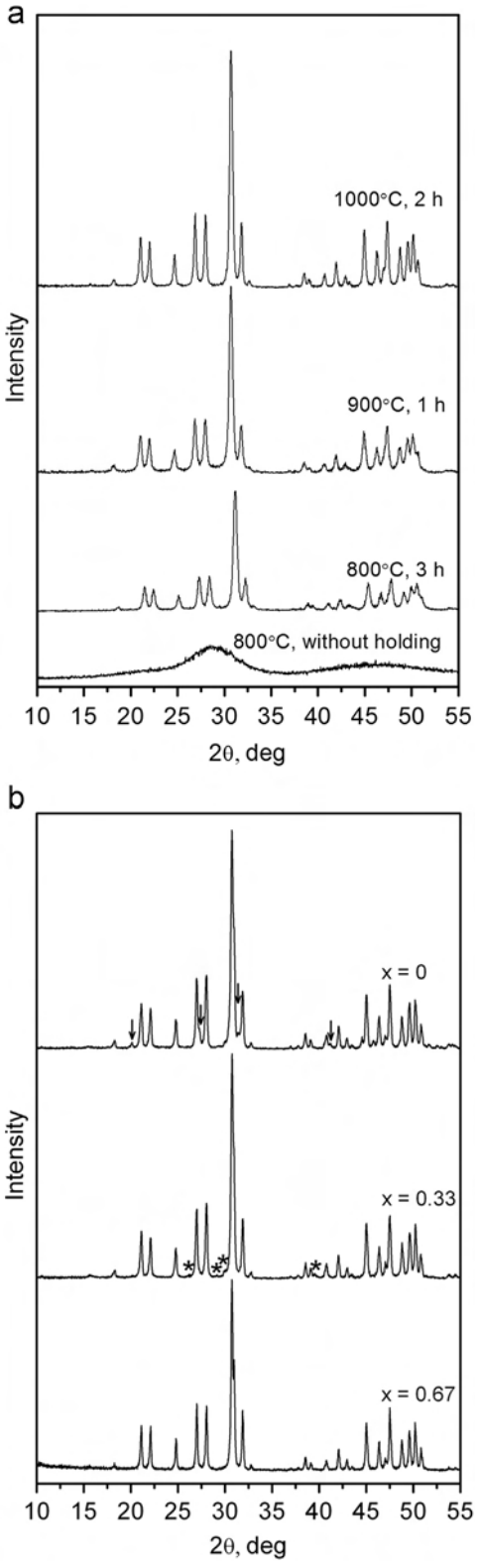

Fig. 2. Typical X-ray diffraction patterns of $La_{9.83}(SiO_4)_{5.5}(AlO_4)_{0.5}O_{2.5}$ sample annealed at different temperatures (a) and undoped $La_{10-x}(SiO_4)_6O_{3-3x/2}$ samples (x=0, 0.33, 0.67) calcined at 1100 °C for 3–8 h (b). ✻ – La_2O_3; ↓– La_2SiO_5.

3.3. Local structure evolution according to IR spectroscopy data

IR spectra of the precipitate dried at 120 °C and then calcined at different temperatures, along with those of precipitate dried at 80 °C, $La(OH)_3$ and silica gel prepared by precipitation under the same conditions and dried at 120 °C are presented in Fig. 3.

Table 1
Some characteristics of samples prepared.

Sample	T (°C)	Phase composition	D_{XRD}, nm	$\Delta d/d$	D_{BET}, nm
$La_{9.33}(SiO_4)_6O_2$	120	Amorphous	–	–	6.4
	800	Apatite	45	$3.8 \cdot 10^{-4}$	34
	900	Apatite	48	$7.4 \cdot 10^{-4}$	85
	1000	Apatite	62	$5.0 \cdot 10^{-4}$	113
	1100	Apatite	119	$4.4 \cdot 10^{-4}$	–
$La_{9.83}(SiO_4)_{5.5}(AlO_4)_{0.5}O_{2.5}$	120	Amorphous	–	–	6.4
	800	Apatite	27	$9.3 \cdot 10^{-4}$	38
	900	Apatite	32	$7.1 \cdot 10^{-4}$	93
	1000	Apatite	81	$5.4 \cdot 10^{-4}$	231
	1100	Apatite	117	$1.4 \cdot 10^{-4}$	–
$La_{9.42}(SiO_4)_{5.5}(AlO_4)_{0.25}O_2$	1000	Apatite	73	$4.8 \cdot 10^{-4}$	90
$La_{10}(SiO_4)_5(AlO_4)O_{2.5}$	1000	Apatite	56	$9.7 \cdot 10^{-4}$	241
$La_{9.67}(SiO_4)_6O_{2.5}$	1100	Apatite, La_2O_3 (1 wt %)	134	$3.2 \cdot 10^{-4}$	–
$La_{10}(SiO_4)_6O_3$	1100	Apatite, La_2SiO_5 (8 wt %)	110	$4.8 \cdot 10^{-4}$	–

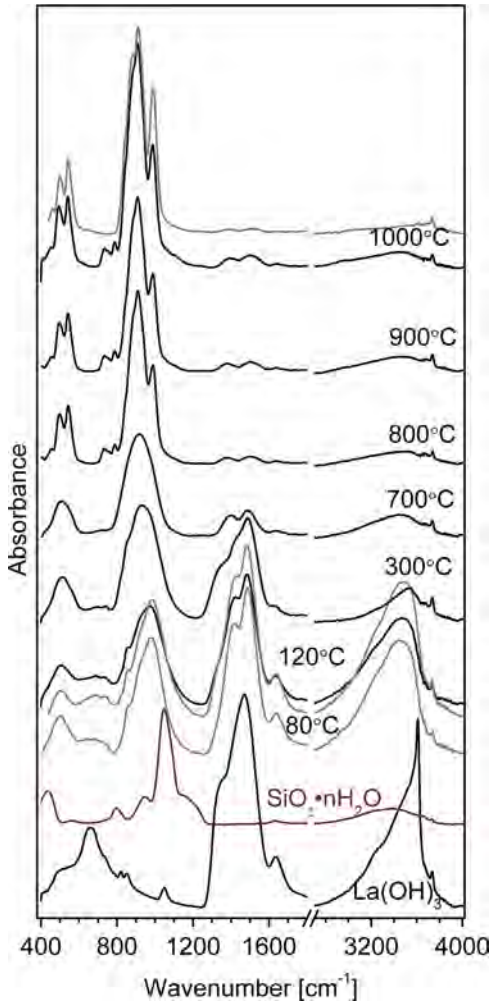

Fig. 3. IR spectra of $La_{9.83}(SiO_4)_{5.5}(AlO_4)_{0.5}O_{2.5}$ (black spectra unless otherwise specified) and $La_{9.33}(SiO_4)_6O_2$ (gray spectra) samples dried in air at 80 and 120 °C and annealed at different temperatures, as well as $La(OH)_3$ and silica gel dried in air at 120 °C.

Lanthanum hydroxide $La(OH)_3$ is formed in the course of precipitation from the water–alcohol solution of lanthanum nitrate, which is revealed by intense absorption bands at 643 and 3607 cm^{-1} in the corresponding spectrum [54]. Along with absorption bands typical for $La(OH)_3$, the spectrum also contains bands in the range of 3000–3600 cm^{-1} and at 1600 cm^{-1} typical for O–H bond vibrations in adsorbed water as well as bands in the ranges 697–730 cm^{-1}, 820–855 cm^{-1} and 1200–1400 cm^{-1} typical for C–O bond vibrations in the CO_3 group of lanthanum oxycarbonate $La_2O_2CO_3$ [55,56], which is due to its formation by interaction of lanthanum hydroxide with CO_2 in humid air. Stable to aggregation opalescent sol is formed under the same conditions from water–alcohol–TEOS solution. Absorption bands typical for silica are presented in the IR spectrum of this sample dried at 120 °C [7].

IR spectra of precipitate obtained from the water–alcohol solution of lanthanum nitrate and TEOS dried at both 80 and 120 °C contain absorption bands with maxima at 965 and 498 cm^{-1}, which can be assigned to Si–O bond vibrations in isolated SiO_4 tetrahedra [7,57,58]. The absorption bands are broadened, which implies a strong structure disordering of silicate compound formed. It is noteworthy that typical Si–O bond vibrations in the isolated SiO_4 tetrahedra are situated at 900–920 cm^{-1} [7,57,58]. The shift of the Si–O band position to 965 cm^{-1} can be caused by strong disordering of the local structure of SiO_4 tetrahedra as well as the presence of some isolated Si_2O_7 groups along with SiO_4 ones in the precipitate [7,57,58], but their identification is not possible due to the band broadening. At the same time, the absence of absorption bands in the region of 1000–1300 cm^{-1} reveals that groups containing more than two connected silicate tetrahedrons are not formed. Besides, absorption bands typical for silica (bands at 464, 552, 799, 950, 1093 and 1180 cm^{-1}) [58] as well as lanthanum hydroxide (bands 643 and 3610 cm^{-1}) or lanthanum oxide (bands in the range of 400–600 cm^{-1}) [54] are not observed in the spectrum (even for samples with the stoichiometry corresponding to the composition outside the range of the homogeneous apatite-type phase existence, such as $La_{10}(SiO_4)_6O_3$ (spectra not shown for brevity)). Therefore, IR spectroscopy data indicate that amorphous lanthanum silicate with the short-range ordering typical for the orthosilicate (silicate containing only isolated SiO_4 tetrahedrons) or ortho-diorthosilicate (silicate containing mainly isolated SiO_4 tetrahedrons and some Si_2O_7 groups), to which apatite-type lanthanum silicates belong, is formed already at the stages of co-precipitation, ageing and drying of the precipitate formed.

Along with absorption bands of Si–O in the isolated SiO_4 tetrahedrons, the spectrum of dried samples also contains bands in the range of 697–730 cm^{-1}, at 820–855 cm^{-1} and in the range of 1200–1400 cm^{-1} typical for C–O bond vibrations in the CO_3 group of lanthanum oxycarbonate $La_2O_2CO_3$ [55] as well as bands in the range of 3000–3600 cm^{-1} and at 1600 cm^{-1} typical for O–H bond vibrations in the water adsorbed at the sample surface.

Unfortunately, due to strong broadening of absorption bands in the spectrum, relatively small amount of aluminum in the

sample and overlapping of bands of Al–O and Al–O–M bonds (M = H, Si, La) with those of Si–O, C–O and OH bonds [7,58], it is difficult to say anything about the state of aluminum in the precipitate of aluminum-doped sample. In general, observed IR spectra of precipitates in the case of undoped and aluminum-doped samples are similar up to 700 °C of calcination temperature.

According to IR spectroscopy data, subsequent thermal treatment of precipitate at 300–1000 °C leads to water removal and decomposition of carbonates. Thus, reduction of the intensity of absorption bands of O–H bond vibrations in water molecules, as well as reduction of intensity and change of profile (in the range of 1200–1400 cm^{-1}) of bands of C–O bond vibrations in the CO_3 group can be observed in the spectrum of sample calcined at 300 °C (Fig. 3). In the Si–O bond vibration region, the shift of absorption bands corresponding to ν_3 Si–O bond vibrations in the regular isolated SiO_4 tetrahedra to the region of smaller wave number values is observed, which points to silicate structure ordering and/or disappearance of Si_2O_7 groups.

In the spectrum of sample calcined at 700 °C, two absorption bands at 507 and 917 cm^{-1} corresponding respectively to ν_4 and ν_3 Si–O bond vibrations in the regular isolated SiO_4 tetrahedra are mainly observed. Absorption bands in the range of 698–850 cm^{-1} of ν_2 and ν_4 C–O bond vibrations in the CO_3-group disappear, and two symmetrical bands typical for monodentate carbonate groups on the oxide surface are present in the range of 1200–1400 cm^{-1}. At the same time in the case of aluminum-modified sample, intense absorption band with maximum at 917 cm^{-1} gets a shoulder in the range of 698–850 cm^{-1} that should be assigned to Al–O vibrations in the isolated AlO_4 tetrahedra in the apatite-type silicate structure [46].

Sample annealing at higher temperatures results in increased intensity and splitting of absorption bands in the range of Si–O and Al–O bond vibrations in the isolated SiO_4 and AlO_4 tetrahedra, respectively. This is caused by further ordering of orthosilicate structure resulting in formation of crystalline apatite-type lanthanum silicate accompanied by splitting of degenerate Si–O mode (ν_3, ν_4) and appearance of forbidden Si–O mode (ν_1, ν_2) as a result of reduction of T_d symmetry in SiO_4 to C_s in silicate apatite structures characterized by the presence of genetic defects (cation vacancies or interstitial oxide ions) [7,57,58].

Generally, according to IR spectroscopy data, the long-range ordering of the lanthanum silicate structure occurs during the precipitate calcination. Thereupon, it is interesting to note that the intermediate and final products of the xerogel thermal treatment in whole retain a "memory" about the initial amorphous orthosilicate structure.

3.4. Local structure evolution according to ^{27}Al and ^{29}Si MAS NMR spectroscopy data

To clarify the features of the formation of aluminum-doped lanthanum silicates, the evolution of the silicon and aluminum local structure was additionally studied by ^{29}Si and ^{27}Al MAS NMR spectroscopy, respectively, for the sample $La_{9.83}(SiO_4)_{5.5}(AlO_4)_{0.5}O_{2.5}$. Corresponding ^{29}Si and ^{27}Al MAS NMR spectra of the sample dried at 80 °C and calcined at 300, 500 and 800 °C are presented in Fig. 4, with some spectra parameters being presented in Table 2.

^{29}Si MAS NMR spectra, especially those of samples calcined at 80–500 °C, are characterized by broad lines and a low value of signal to noise ratio due to a low ^{29}Si isotope content (< 0.37 wt%) and amorphous state of samples leading to a broad range of Si states in sample due to variation of their local atomic environment. Nevertheless, they provide additional information about evolution of the local silicon environment at the initial stages of synthesis. In the ^{29}Si MAS NMR spectrum of the sample dried at 80 °C, a broad peak is observed in the range of −(73–89) ppm (Fig. 4a). According to the spectrum deconvolution, this peak is a superposition of two lines with chemical shifts $\delta = -78$ ppm and $\delta = -83$ ppm and intensity ratio of 3/2, corresponding to SiO_4 tetrahedra of Q^1 and Q^0 types, respectively (Table 2) [48,59,60]. The presence of SiO_4 tetrahedra of Q^1 type in the xerogel spectrum is in agreement with IR spectroscopy data and confirms the presence of some Si_2O_7 groups along with SiO_4 ones in the initial precipitate formed. There is no peak in the range of −(90–130) ppm, which, in turn, confirms the absence of more condensed silicate tetrahedrons.

The sample calcination at 300–500 °C results in decrease of the signal at $\delta = -83$ ppm, typical for SiO_4 tetrahedra of Q^1 type, up to its disappearance (Table 2). Thus, the intensity ratio of the peaks with chemical shifts at $\delta = -78$ ppm and $\delta = -83$ ppm is 7/3 in the spectrum of sample calcined at 300 °C, while there is only one broad peak at $\delta = -78$ ppm in the spectrum of sample calcined at 500 °C. In the ^{29}Si MAS NMR spectrum of the crystalline sample treated at 800 °C, only one intense narrow peak at $\delta = -77.0$ ppm corresponding to SiO_4 tetrahedra of Q^0 type is observed as well, with peak narrowing and shifting to be caused by sample crystallization. This is also in accordance with IR spectroscopy data, which indicate the presence of only isolated SiO_4 tetrahedra in samples treated at 500–800 °C.

In the ^{27}Al MAS NMR spectrum of sample dried at 80 °C, two intense peaks with $\delta = 6.3$ ppm and $\delta = 56.3$ ppm corresponding to octahedral AlO_6 and tetrahedral AlO_4 units as well as a low-intensity peak with $\delta = 32$ ppm, which can be assigned to five-coordinated AlO_5 units, are present [59,61]. Following Iuga, who carried out a detailed study by means of ^{27}Al MAS NMR and XRD methods of the amorphous and crystalline lanthanum–aluminates of the composition $(1-x)Al_2O_3 \cdot xLa_2O_3$ $(0 < x < 0.7)$ prepared by sol–gel synthesis [61], one can conclude that aluminum is incorporated in the structure of the amorphous precursor formed in the course of co-precipitation followed by the residue drying at 80 °C, with the four-, five- and six-coordinated units being formed by OH^- and O^{2-} ions as well as water molecules. The presence of low-coordinated aluminum atoms already in xerogel dried at 80 °C, in contrast to the calcination temperature range of 300–600 °C required for this phenomenon in the case of La–Al–O sol–gel samples as noted by Iuga [61], indicates the interaction of the component during precipitation and drying stages.

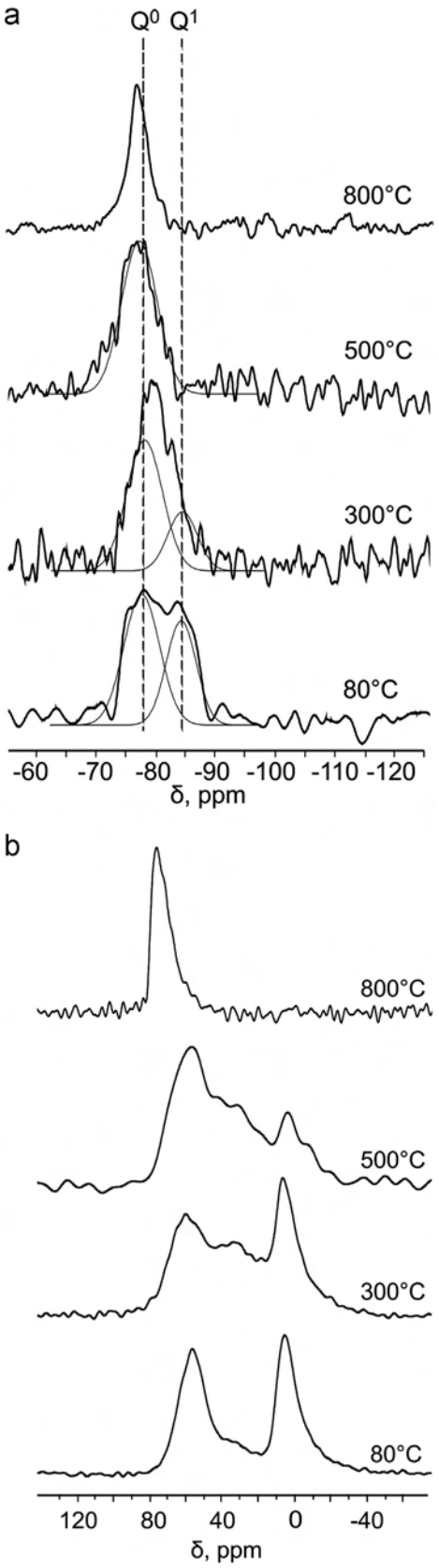

Fig. 4. ^{29}Si MAS NMR (a) and ^{27}Al MAS NMR (b) spectra of $La_{10-x}(SiO_4)_{5.5}(AlO_4)_{0.5}O_{2.75-3x/2}$ sample dried in air at 80 °C and annealed at 300, 500 and 800 °C.

Table 2
^{29}Si MAS NMR and ^{27}Al MAS NMR data.

Treatment temperature (°C)	Si species			Al species		
	Coordination	δ (ppm)	I (%)	Coordination	δ (ppm)	I (%)
80	Q^0	−78	60	AlO_6	6.3	40
	Q^1	−83	40	AlO_5	32	10
				AlO_4(A)	56.3	50
300	Q^0	−78	70	AlO_6	6.3	35
	Q^1	−83	30	AlO_5	32	20
				AlO_4 (A+B)	59	45
500	Q^0	−78	100	AlO_6	6.3	20
				AlO_5	32	30
				AlO_4 (B)	61	50
800	Q^0	−77	100	AlO_4	76	100

Taking into account the hydration effect observed by Iuga for the amorphous samples treated at intermediate temperatures, it can be also assumed that the six-coordinated AlO_6 units present in the xerogel are due to a part of four-coordinated AlO_4 units remain accessible to water molecules and may be located at the surface of the primary particles forming the amorphous precursor.

Subsequent thermal treatment of xerogel up to 500 °C leading to its dehydration decreases the intensity of peak of six-coordinated aluminum and increases that of penta-coordinated aluminum, whereas peaks of four-coordinated aluminum remains practically constant (Table 2). This is accompanied by the shift of position of the peak corresponding to tetrahedral AlO_4 units to the weak field up to $\delta=61$ ppm. In the ^{27}Al MAS NMR spectrum of the crystalline sample calcined at 800 °C, the only peak characterized by $\delta=76$ ppm is observed, which corresponds to tetrahedral AlO_4 units with a great local tetrahedron distortion, typical for aluminum in silicon sites in the apatite-type silicate structure [48].

The alteration of the peak corresponding to tetrahedral AlO_4 units depending on the temperature of the sample treatment at 80–500 °C indicates that this peak is a superposition of two peaks (Table 2). The former one (peak A), characterized by $\delta=56.3$ ppm, corresponds to regular tetrahedral AlO_4 units formed during the precipitation followed by residue drying. The latter one (peak B) characterized by $\delta=61$ ppm and great local tetrahedron distortion is due to four-coordinated AlO_4 sites formed during sample calcinations. In this respect, some decrease of the intensity of peak corresponding to tetrahedral AlO_4 units observed at 300 °C (Table 2) can be caused by the strong distortion of their coordination sphere, which may not be seen in ^{27}Al MAS NMR spectra of amorphous sample. The relative proportion of the peaks A and B in the spectrum of sample calcined at 300 °C is difficult to estimate. However, according to the spectrum analysis, the peak A is practically absent in the spectrum of sample calcined at 500 °C. The further shift of the peak corresponding to tetrahedral AlO_4

units up to 76 ppm in the spectrum of sample calcined at 800 °C is caused by sample crystallization.

The formation of AlO_4 units with the great local distortion in the course of sample calcination is in good agreement with IR spectroscopy data clearly indicating the appearance of the absorption bands of Al–O vibrations in isolated AlO_4 tetrahedra in the apatite-type silicate structure at 698–850 cm^{-1} in the spectrum of the aluminum-doped sample calcined at temperatures higher than 500 °C.

Therefore, according to ^{29}Si and ^{27}Al MAS NMR data, the thermal treatment of xerogel at first results in ordering of the amorphous precursor local structure by transformation of Si_2O_7 groups into regular SiO_4 tetrahedra as well as conversion of six- to penta-coordinated aluminum in the course of dehydration processes, which is accompanied by the strong distortion of present tetrahedral AlO_4 units. The complete transformation of six- to penta-coordinated aluminum to form AlO_4 units occurs at temperatures higher than 500 °C and seems to be accompanied by the precursor crystallization into doped apatite-type silicate.

3.5. Low-temperature nitrogen adsorption data

Genesis of lanthanum silicate texture was studied by the method of low-temperature nitrogen adsorption for dried xerogel calcined at temperatures up to 1000 °C. According to the data obtained, the produced xerogel possesses high specific surface area S_{BET} and specific volume of pores V, which are about 170 m^2/g and 0.6 cm^3/g for xerogel calcined at 120 °C, respectively (Fig. 5a and b). Besides, it is characterized by the mesoporous structure with the pore size varying in the range from 5 to 70 nm (Fig. 5c, SI1).

Xerogel calcination in the temperature range of 300–1000 °C results in decrease of the specific surface area and pore volume, with four specific regions being detected (Fig. 5). A sharp decrease of specific surface area accompanied by considerable decrease of pore volume is observed when xerogel is calcined at 300 °C. At the same time, the pore size distribution is not changed. No drastic changes of specific surface area and pore volume were observed under further calcination up to 700 °C, with pore size distribution being only slightly shifted to larger values. On the contrary, annealing at 800–900 °C results in more substantial decrease of specific surface area and, especially, pore volume accompanied by significant change in the pore size distribution. The latter is represented by meso- and macropores with sizes varying in the range from 10 to 120 nm. Finally, calcination at higher temperatures is not accompanied by any considerable change in the textural characteristics.

Assuming that a density of the amorphous lanthanum orthosilicate/ortho-diorthosilicate precursor formed in the course of co-precipitation is close to the density of silicate with the apatite structure (5.4–5.5 g/cm^3), one can estimate the size of primary particles D_{BET} based on the adsorption data by the relation

$$D_{BET} = 6000/(\rho \cdot S_{BET}),$$

where ρ is density (g/cm^3); S_{BET} is specific surface area (m^2/g).

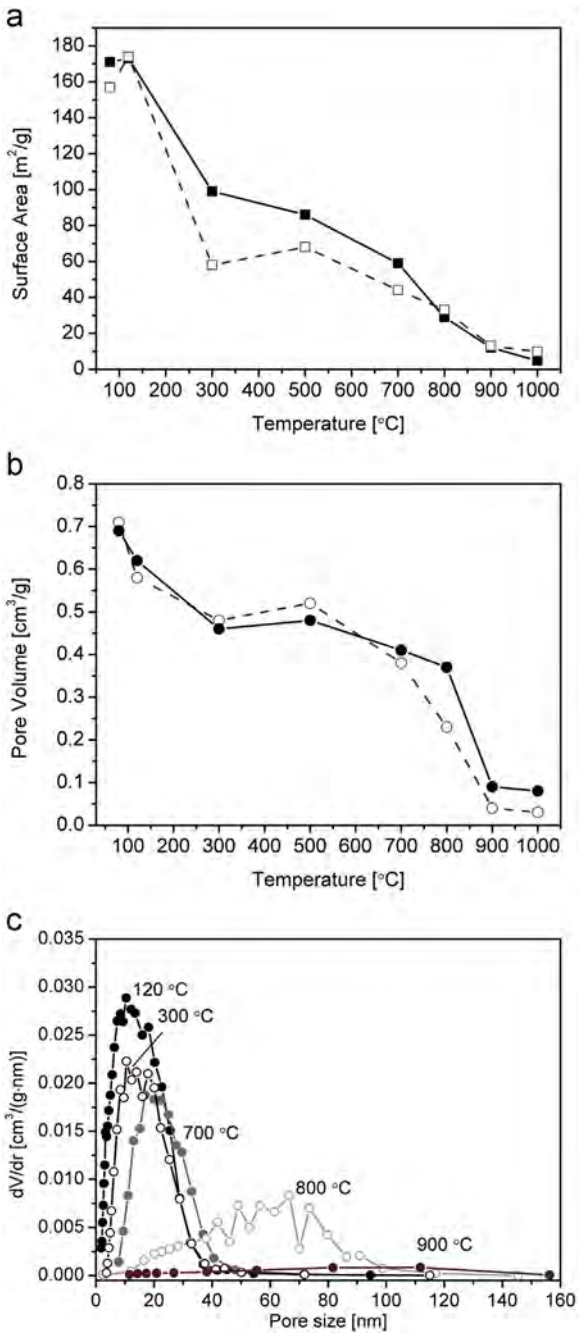

Fig. 5. Typical dependences of specific surface area (a) and specific volume of pores (b) on calcination temperature exemplified by those of $La_{9.33}(SiO_4)_6O_2$ and $La_{9.83}(SiO_4)_{5.5}(AlO_4)_{0.5}O_{2.5}$ samples as well as corresponding pore size distribution curves at different calcination temperatures exemplified by those of $La_{9.83}(SiO_4)_{5.5}(AlO_4)_{0.5}O_{2.5}$ sample (c).

The estimated average size of particles for different samples is ca 6 nm (Table 1). Taking into account that the total surface area of primary particles in agglomerates can be inaccessible for nitrogen adsorption, this may be a slightly underestimated figure, and, thereby, is in good agreement with the typical size of primary particles of hydroxides obtained by precipitation (3–5 nm) [52]. Thereby, according to the nitrogen adsorption data, the size of primary particles forming xerogel amounts to the one of sol particles formed during precipitation under great oversaturation

with respect to the forming phase, which is typical for amorphous precipitates of slightly soluble hydroxides and oxides [52].

The xerogel calcination results in increase of particles size estimated from the adsorption data (Figure SI2). For instance, the average particle size of sample calcined at 500 °C is about 15 nm. The calcination at 800 and 900 °C results in the particles size increase up to about 34 and 89 nm, respectively. The observed increase of particles size estimated from the adsorption data can be caused by formation of compact agglomerates of primary particles, growth of primary particle size, amorphous precursor crystallization into primary crystals as well as formation of secondary crystals. To specify this, TEM spectroscopy study was additionally carried out.

3.6. Transmission electron microscopy data

The typical micrographs of samples at different stages of preparation are presented in Figs. 6–10. According to TEM data, only amorphous phase was observed in xerogels of both undoped and aluminum-doped samples (Fig. 6a). According to EDX analysis, the chemical composition of the amorphous precursor includes silica and lanthanum as well as aluminum in the case of doped sample (Fig. 6b and c). Besides, the local composition of the sample does not change essentially from point to point. Therefore, TEM with the EDX analysis additionally confirms the interaction of component during precipitation and drying stages to form the amorphous lanthanum silicate precursor already in the course of precipitation.

Unfortunately, the xerogel structure under conditions of TEM observations is very unstable, which hinders its detailed studies at high resolution. However, TEM micrographs at relatively low resolution show that obtained xerogels consist of 10–50 nm agglomerates of amorphous primary particles with typical sizes in the range of 3–6 nm (Fig. SI3). The sample calcined at 500 °C is still amorphous and consists of porous particles with sizes of 20–300 nm, which seem to be formed by rather compact agglomerates of primary particles (Fig. 7).

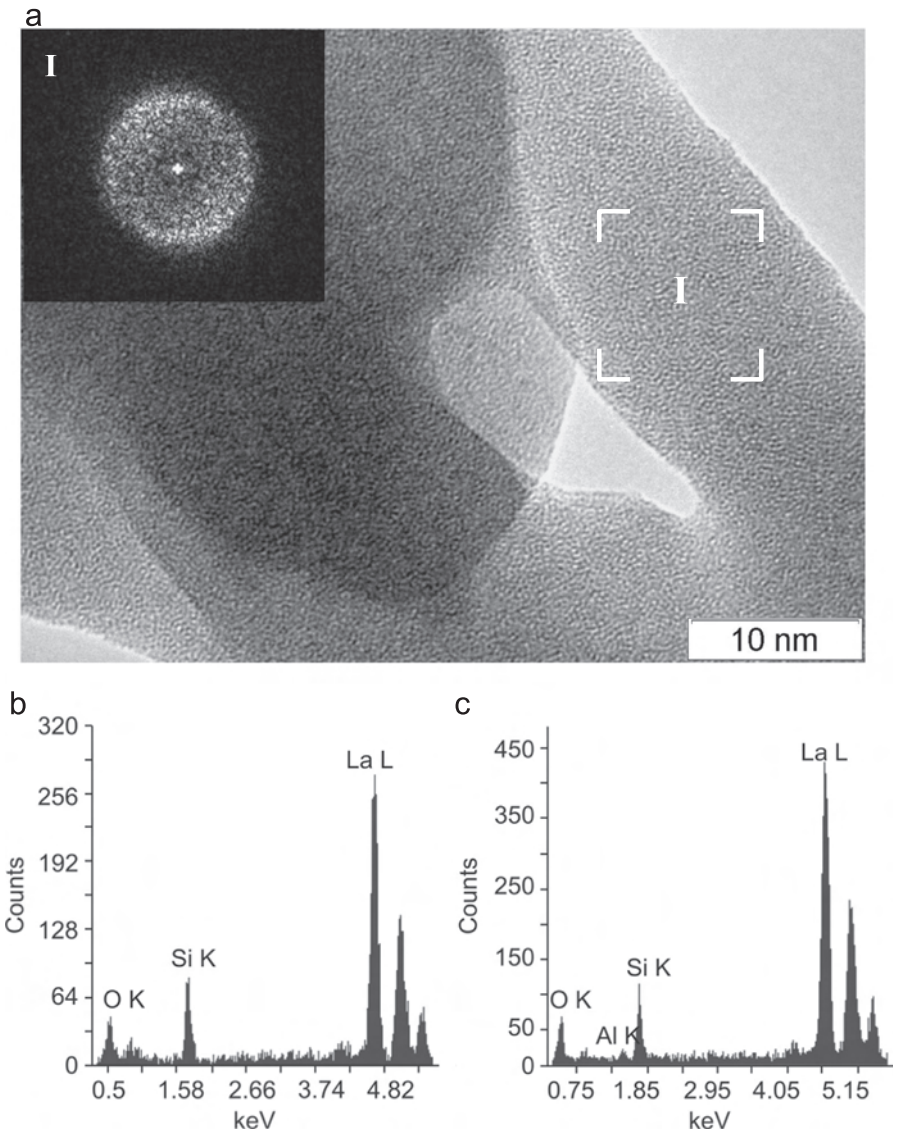

Fig. 6. Typical HRTEM image of xerogel dried at 120 °C exemplified by that of undoped sample, corresponding Fourier transformation image (inset) (a) as well as typical EDX data of amorphous particles of undoped (b) and aluminum-doped samples (c).

The sample calcined at 800 °C is formed by crystalline apatite particles with sizes in the range of 30–200 nm having irregular shapes and pores (Fig. 8), which appear to be formed by agglomerates of primary particles of lanthanum silicate precursor in the course of precursor crystallization. The particle size of about 34–38 nm estimated from the adsorption data on the assumption of spherical particles agrees well with the typical size of elements of these irregular-shaped particles. In this respect, it should be also noted that X-ray particle size estimated from diffraction peaks broadening seems to correspond to the average size of ordered regions of apatite particles agglomerates limited by elements of their texture – pores, domain boundaries, etc. Thereby, low-temperature nitrogen adsorption, TEM and XRD data indicate that textural characteristics of crystalline apatite-type lanthanum silicates are defined by textural features of amorphous precursor, controlled by the size and morphology of primary particle agglomerates. It is also interesting that along with well crystalline apatite particles some amorphous ones of lanthanum silicate precursor as well as partially crystallized apatite particles were also observed in the sample calcined at 800 °C, with the composition of the crystalline and amorphous particles being practically the same according to EDX analysis (Fig. 9, SI4)

Only crystalline particles with typical sizes of 100–300 nm consisting of stacked crystallites with size of 30–100 nm are observed in samples calcined at 1000 °C (Fig. 10). Some closed pores are observed in these particles as well as in the sample calcined at 800 °C, which seem to agree with the X-ray particle size of 30–55 nm.

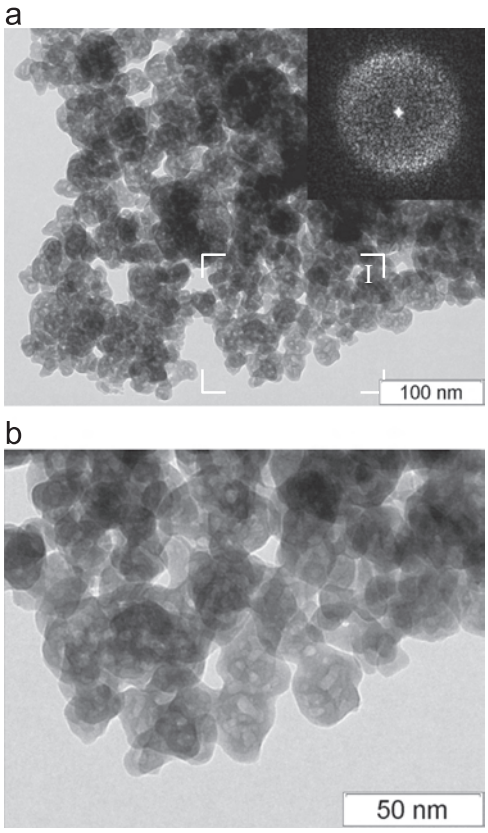

Fig. 7. Typical TEM images of sample calcined at 500 °C exemplified by that of undoped sample (a,b), corresponding Fourier transformation image (inset); the image (b) is a higher resolution one of a fragment.

4. Discussion

4.1. Tentative mechanism of lanthanum silicate formation and crystallization

The formation process and crystallization mechanism of many compounds prepared by the precipitation/co-precipitation method can be considered in the relation to classical molecular-kinetic theory, which is based on ideas of solutions and solubility of substances and the Gibbs–Volmer concepts concerning nucleation and growth of crystals [52,64–68]. However, it was found that the formation and crystallization of slightly soluble amorphous precipitates of hydroxides of transition and some other trivalent metals cannot be fully described in terms of classical theory via the stage of dissolution [52,69–73]. To explain the behavior of such precipitates, Buyanov and Krivoruchko developed a theory of formation of amorphous precipitates of slightly soluble hydroxides and oxides and their crystallization via the mechanism of "oriented accretion" [52].

The peculiarities of the structure and texture of apatite-type lanthanum silicates genesis revealed in the present study indicates that the apatite-type lanthanum silicate formation in the given conditions occurs via the mechanism of "oriented accretion". For one thing, IR spectroscopy and NMR data indicate that amorphous lanthanum silicate with the local atomic ordering typical for the ortho-diorthosilicate, notably silicate containing isolated SiO_4 tetrahedra and some Si_2O_7 groups, to which apatite-type lanthanum silicates can be ascribed, is formed already at the stages of co-precipitation, ageing and drying of the residue formed. Groups with more condensed SiO_4 tetrahedra are not formed in the precipitate. This indicates that the interaction between constituents under precipitation occurs at the level of hydroxocomplexes or at the molecular level at the stage of polycondensation leading to formation of a set of "deadlock" polyhydroxocomplexes, which give rise to primary particles [52,71].

The formation of amorphous ortho-diorthosilicate phase during residue drying as a result of interaction between primary particles of individual hydroxides $SiO_2 \cdot nH_2O$ and $La(OH)_3$ produced during co-precipitation, as some researchers assume [34,35,53], seems unlikely in our case. The formation of primary 3–6 nm particles of individual hydroxides formed under great oversaturation with respect to the forming phase and their aggregates composed both from primary particles of different and the same chemical nature usually results in formation of corresponding oxides in the course of aging or thermal treatment of the residue [52,71–74]. At the same time, the solid-state reaction between components of the mechanical mixture of silica and lanthana to form silicate with the apatite structure was shown to take place at temperatures exceeding 1000 °C [75]. Mixing of silica and lanthanum oxide or its precursor as a result of the precipitate or gel formation from solution allows reducing the temperature of their interaction to 800–850 °C [32,76,77].

On the second hand, the process of precipitate "ageing" starts immediately after formation of primary particles. However,

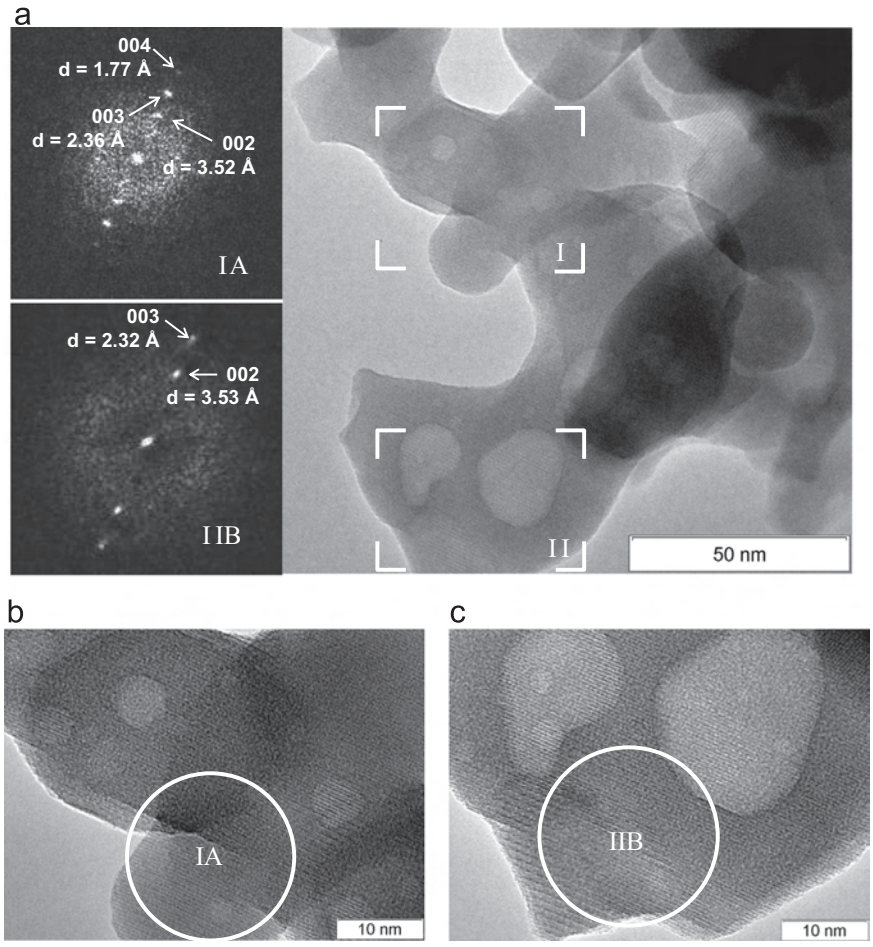

Fig. 8. Typical HRTEM images of sample calcined at 800 °C exemplified by that of undoped sample (a,b,c) and corresponding Fourier transformation image (insets) from fragments marked IA and IIB in images (a) and (b), respectively; the images (b) and (c) are higher resolution ones of fragments marked, respectively, I and II in image (a).

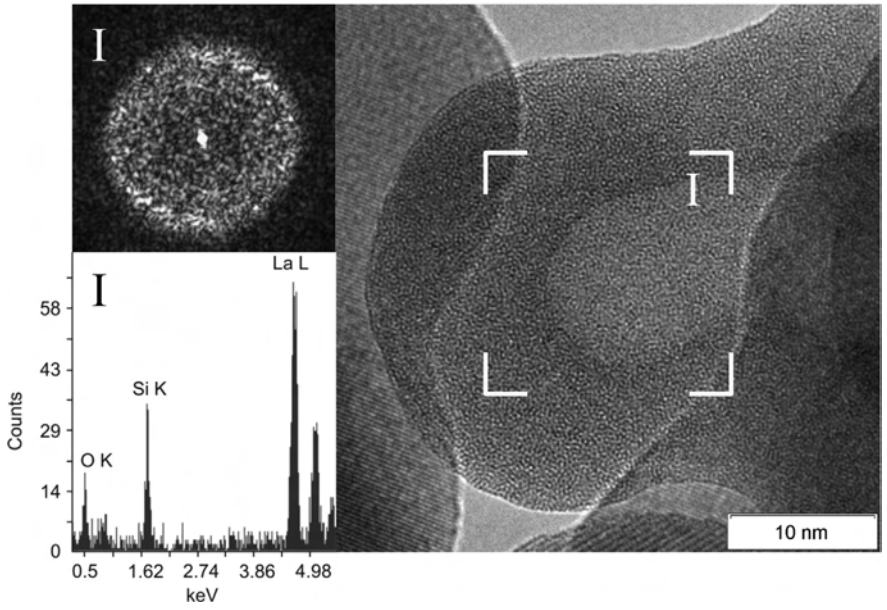

Fig. 9. HRTEM image of an amorphous particle in sample calcined at 800 °C and corresponding Fourier transformation image (inset) and EDX data (inset) from fragment marked I in the image.

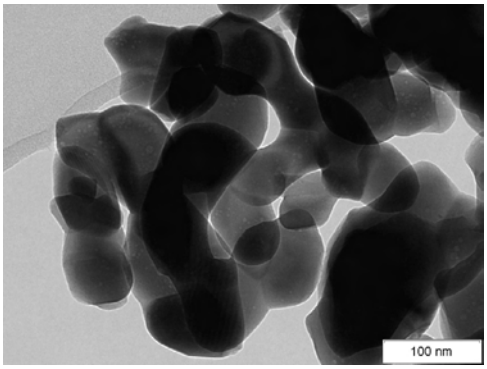

Fig. 10. Typical TEM image of sample calcined at 1000 °C exemplified by that of undoped sample.

according to the nitrogen adsorption and TEM data, the size of primary particles forming xerogel is close to that of typical sol particles formed during precipitation, which indicates that dissolution of the precipitate formed can be hampered during its aging in mother solution. Besides, crystallization of the amorphous lanthanum silicate does not occur in the course of precipitate aging in mother solution at ambient conditions as well as drying up to 120 °C, but only in the course of the subsequent thermal treatment of the xerogel up to 800 °C, with intermediate and final products of ageing preserving a "memory" about the initial sample structure. The long-range ordering in the bulk of primary particles may be hindered by water molecules formed during precipitate ageing. They seem to remain in the polymeric structure of primary particles occupying a part of cation positions (for more details, see Section 4.2). This assumes that the formation of the crystalline structure of the apatite-type lanthanum silicate occurs inside primary particles via the rearrangement of their polymer structure rather than via dissolution of the primary particle substance [52]. Simultaneous presence of crystalline apatite particles, partially crystallized apatite particles and amorphous ones of lanthanum silicate precursor during crystallization with similar composition, according to TEM with EDX data, also confirms the possibility of the lanthanum silicates crystallization via the mechanism of "oriented accretion" [52].

Crystallization of the apatite-type lanthanum silicates via the mechanism of "oriented accretion" supposes a low solubility ($pK_{sp} < 30$) of the lanthanum silicate under the conditions used. Unfortunately, we have not found a solubility product (sp) data for apatite-type lanthanum silicates in literature. However, it was shown that in the La_2O_3–CaO–SiO_2–H_2O–CO_2 system, the La-bearing hydroxylapatite and britholite $Ca_4La_6(SiO_4)_6(OH)_2$ are considerably less soluble phases than lanthanum hydroxides or carbonates [78]. The lanthanum concentration in solutions determined in this work for both precipitates $\lg[La^{3+}]$ was less than −(10–15), whereas $\lg[La^{3+}]$ is about −5.22 and −6.68 in the case of $La(OH)_3$ (pK_{sp} = 19.4–20.89) and $La_2(CO_3)_3$ (pK_{sp} = 33.4), respectively. This confirms the possibility of the lanthanum silicate crystallization via the "oriented accretion" mechanism. The absence of primary particles growth during aging in mother solution also indirectly confirms a low solubility of the lanthanum silicate under the conditions used.

4.2. About the polymeric structure of amorphous lanthanum silicate precursor and its rearrangement

In the present study, we did not aim at elucidation of the composition and structure of key (or "deadlock" [52]) polyhydroxocomplexes as well as polymeric structure of primary particles formed thereof. However, the set of data including IR, ^{29}Si and ^{27}Al MAS NMR spectroscopy, and EDX analysis indicates that the polymeric structure of primary particles is formed by lanthanum and silicon polyhydroxocomplexes as well as aluminum ones in the case of doped samples or even by some mixed polyhydroxocomplexes like $[La_mSi_xAl_y(OH)_n(H_2O)_p]^{(3m+4x+3y-n)+}$.

It is interesting to note that lanthanum hydroxide is an easily crystallizing hydroxide and can be simply formed as crystalline phase in the course of precipitation via dissolution of the primary particle substance [79,80]. The hexagonal structure of $La(OH)_3$ belonging to P63/m space group contains stacked nine-fold coordinated polyhedra with empty columns between them [81]. It was shown earlier that tetrahedral SiO_4 and AlO_4 units can be relatively easily incorporated in such structure without its considerable rearrangement [49], assuming a structural "compatibility" of the polyhydroxocomplexes during the primary particle formation [52]. In this respect, it can be assumed that the polycondensation of lanthanum polyhydroxocomplexes in the presence of silicon and aluminum ones during co-precipitation results in the formation of the polymeric structure similar to that of lanthanum hydroxide with columns to be partially filled by silica and aluminum. The difference in acid–base properties of individual lanthanum and silicon hydroxides should favor such interaction of the polyhydroxocomplexes. Water molecules formed due to interaction of polyhydroxocomplexes seem to remain in the polymeric structure of primary particles occupying a part of cation positions, which hinders the long-range ordering in the bulk of primary particles.

The presence of some Si_2O_7 units in the dried precipitate indicates that the initial polymeric structure of the amorphous precursor formed during co-precipitation, being similar to that of $La(OH)_3$, contains quite wide isotropic (in *ab* plane) empty columns (or channels) generated by stacking of LaO_9 polyhedra, with La–La distances between opposite La atoms being equal (~6.55 Å as in $La(OH)_3$). In the case of $La(OH)_3$, LaO_9 polyhedra, with an edge length being ~3 Å, form channels with the width of ~5.2 Å. In such large channels both SiO_4 (the edge length is ~2.7 Å) and Si_2O_7 units (the length of two SiO_4 tetrahedra sharing a corner is ~5.2 Å) can be located. This conforms to the fact that linear dimension of coordination polyhedra for cations with a large radius do not match to the edge length of SiO_4 tetrahedron, but is proportional to the length of Si_2O_7 group [82,83]. According to IR and ^{29}Si MAS NMR spectroscopy data, the rearrangement of the polymeric structure of amorphous precursor in the course of sample calcination results in the channel distortion accompanied by Si_2O_7 groups destruction to form regular SiO_4 one, with the formation of the orthosilicate local structure being completed during thermal treatment up to 500 °C.

It is also interesting that, according to ^{27}Al MAS NMR data, a part of aluminum atoms is present in the xerogel as octahedral AlO_6 units, while another part is present as AlO_4 tetrahedra. The presence of low-coordinated aluminum atoms in the amorphous lanthanum aluminates was earlier revealed by Iuga [61]. In accordance with Iuga, AlO_4 tetrahedra are located in the volume of the primary particles, while octahedral AlO_6 units are due to a part of four-coordinated AlO_4 units remain accessible to water molecules. In this connection, the latter may be located both at the surface and in the bulk of primary particles forming the amorphous precursor. Formation of four-coordinated AlO_4 units in amorphous lanthanum aluminates [61] and lanthanum aluminosilicates may be caused by the similarity of the polymeric structure of the amorphous precursor and lanthanum hydroxide, where lanthanum is nine-coordinated. This does not require considerable changes in the structure of the precipitate. Incorporation of octahedral AlO_6 units into the polymeric structure of amorphous lanthanum silicate, for example, leading to formation of perovskite-like structure of $LaAlO_3$ containing lanthanum with coordination number 12, seems to be hindered due to the need of considerable changes in the structure of amorphous precipitate. In the whole, this points out some similarity of genesis of structures of the apatite-type lanthanum silicates and lanthanum aluminates at early stages in the course of co-precipitation. However, in the case of aluminum-doped lanthanum silicates, only some structural rearrangement accompanied by AlO_4 unit distortion is observed, whereas in the case of lanthanum aluminates with equimolar composition, serious changes occur in both lanthanum and aluminum local structure [61].

Finally, one can note that, according to IR spectroscopy data, dried precipitate contains lanthanum oxycarbonates characterized by the layer-like structure built up of slabs of $\left(La_2O_2^{2+}\right)_n$ and carbonate ions occupying the interlaminar space [55,81]. The $\left(La_2O_2^{2+}\right)_n$ layers have C_3 symmetry and can be described as consisting of linked seven-fold LnO_7 polyhedra [81]. Thus, $\left(La_2O_2^{2+}\right)_n$ structural fragments can be assumed to be present in the xerogel formed as typical for similar hexagonal structures of lanthanum oxide and apatite-type lanthanum silicate [36,51,81], which are produced due to dehydration and oxolation in the residue empty columns generated by LaO_9 polyhedra in the amorphous precipitate structure in the course of precipitate ageing or drying. The lanthanum oxycarbonates presence in the xerogels suggests that precipitate drying under air is accompanied by the carbonation. In the course of drying under air, CO_2 molecules get embedded between $\left(La_2O_2^{2+}\right)_n$ pseudo-layers of the polymeric primary particle structure, for example, within particle interfaces, additionally forming structural elements typical for $La_2O_2CO_3$.

All these results imply that crystalline apatite structure forms by rearrangement of the polymeric structure of primary particles of amorphous lanthanum silicate during thermal treatment due to dehydration and decomposition of carbonates. In this respect, the exothermic effect observed during sample annealing in the non-isothermal mode within the temperature range of 860–920 °C is indeed caused by crystallization of silicon apatite. At the same time, Li's assignment of the broad exothermic effect in the 160–520 °C range to interaction between lanthana and silica domains producing amorphous oxy-apatite phase [34], is not supported by our results revealing formation of the amorphous lanthanum silicate precursor already at the initial stages of synthesis. Besides, according to the data of MS analysis of gas phase during the thermal analysis, the sample mass loss is caused by the dehydration as well as decomposition of carbonates in this temperature range, which requires heat supply. Exothermic effect within the range of 160–520 °C is likely caused by ordering of amorphous ortho-diorthosilicate/orthosilicate structure via rearrangement of the polymeric structure of primary precipitate particles [52].

It should be also noted that, according to the XRD data, calcination of xerogels of samples with compositions falling within the range of homogeneous apatite-type phase existence does not result in formation of secondary phases – $La(OH)_3$, La_2O_3, $LaAlO_3$, Al_2O_3 etc. In the case of samples with the stoichiometry corresponding to the composition outside this range, particularly with the lanthanum excess, the thermal treatment first results in formation of some La_2O_3 phase along with the apatite one, while La_2SiO_5 phase forms due to subsequent solid state reaction between La_2O_3 and apatite at higher temperatures. This agrees with formation of the binary (La–Si containing) or ternary (La–Si–Al containing) precursor of variable composition in the course of co-precipitation and drying, which transforms to nonstoichiometric apatite-type lanthanum silicate without decomposition into individual oxides during subsequent thermal treatment. Such a transformation can be accompanied by formation of La_2O_3 phase in the case of samples with the stoichiometry corresponding to the composition outside the region of homogeneity.

4.3. Genesis of lanthanum silicate texture

Formation of crystalline lanthanum silicate phase on the basis of oriented growth mechanism suggests that the size of primary silicate crystals is approximately equal to the size of primary particles formed during precipitation [52], which agrees with the results of low-temperature nitrogen adsorption and TEM data. Results of low-temperature nitrogen adsorption and TEM data suggest that during co-precipitation from solution weakly bound agglomerates of small primary particles of amorphous lanthanum ortho-diorthosilicate/orthosilicate precursor are formed. During the drying step (up to 120 °C) under conditions minimizing alteration of the hydrogel texture, contacts between the primary particles are strengthened and the initial texture characterized by high specific surface area and specific volume of pores is formed. In the course of subsequent thermal treatment up to 300 °C, the aggregate compacting accompanied by intergrowth of primary particles occurs, while number of contacts between the particles remains unchanged. This results in decrease of the specific surface area and volume of pores, while the pore size distribution remains unaffected. Subsequent calcination up to 700 °C does not appreciably affect the surface area and pore structure of samples. Thereby, formation of the supramolecular structure of amorphous lanthanum orthosilicate is mainly completed during thermal

treatment in the range of 120–500 °C. It is the amorphous precursor texture that defines textural characteristics of crystalline apatite-type lanthanum silicates formed.

During annealing in the range of 700–900 °C, processes of amorphous orthosilicate precursor crystallization occur, being accompanied by considerable decrease of the specific surface area and pore volume of samples as well as by significant change in the pore size distribution. According to TEM data, the shape of apatite crystalline particles resembles that of aggregates in the amorphous sample. Taking into account that the main weight loss of samples is completed below 700 °C (Fig. 1) and assuming that density of the amorphous lanthanum orthosilicate precursor is close to the one of crystalline apatite-type lanthanum structure, one can conclude that the precursor crystallization occurs with insignificant change of phase volume (Pilling-Bedworth ratio $\Delta \approx 1$) and, thus, without dispersion of a new phase. This feature along with the presence of amorphous particles of lanthanum silicate precursor as well as partially crystallized apatite particles simultaneously with well crystalline apatite during crystallization implies that crystallization nuclei are formed in the bulk of amorphous particles within mentioned temperature range as a result of precursor polymeric structure rearrangement. The irregular shape of formed apatite crystalline particles indicates that the formation rate of secondary crystal is higher than those of crystallization centers and nuclei. Some pores present in the amorphous aggregates remain in the formed crystalline particles. The additional oriented stacking of crystallization nuclei resulting in formation of bigger secondary crystals is accompanied by decrease of specific surface area and pore volume.

During further annealing within the temperature range of 900–1000 °C specific surface and porosity of samples remain practically unchanged, which is associated with completed crystallization of amorphous solid in the course of annealing at 800–900 °C and absence of the phase transformations in crystalline lanthanum silicate thus produced. Prolonged annealing of the sample at 1000 °C or at higher temperatures results in sintering of crystalline lanthanum silicate accompanied by decline of sample surface area and porosity.

Therefore, the results obtained suggest that textural characteristics of prepared crystalline silicates with the apatite structure are in general determined by those of amorphous precursor formed during xerogel thermal treatment in the range of 120–500 °C, which in turn results from the size and morphology of primary particle agglomerates. The results presented indicate that textural characteristics of lanthanum silicates obtained by co-precipitation could in principle be modified, for instance, by using proper surfactants, varying conditions of ageing and thermal treatment of precipitates to control the formation rates of secondary crystal, crystallization centers and nuclei. Such approach to control particle agglomeration and obtain fine apatite-type lanthanum silicate powders was attempted by Yang by using a dispersant additive [35]. Unfortunately, conditions of synthesis used in [35] did not result in higher dispersion of lanthanum silicate formed. Nevertheless, this work shows the possibility of controlling textural characteristics of lanthanum silicates produced by co-precipitation.

5. Conclusions

Peculiarities of genesis of the structure and texture of apatite-type lanthanum silicates in the course of synthesis via co-precipitation method were revealed. In particular, an amorphous lanthanum silicate with the local atomic ordering typical for ortho-diorthosilicate was shown to be formed already at the stages of components co-precipitation, ageing and drying of the precipitate formed. In the case of aluminum doped apatite-type silicates, the initial formation of amorphous lanthanum ortho-diorthosilicate precursor containing aluminum atoms in the polymeric structure was established. The growth of size of primary particles forming precipitate as well as crystallization of the amorphous lanthanum silicate was shown not to occur in the course of precipitate aging in mother solution at ambient conditions as well as drying up to 120 °C, but only in the course of subsequent thermal treatment of xerogel up to 800 °C, with intermediate and final products of ageing preserving a "memory" about the initial sample structure.

The peculiarities of the structure and texture of apatite-type lanthanum silicates genesis revealed here suggest that the apatite-type lanthanum silicates formation in the given conditions occurs via the mechanism of "oriented accretion". The polycondensation of lanthanum polyhydroxocomplexes in the presence of silicon and aluminum ones during co-precipitation was assumed to result in the formation of primary particles with the polymeric structure similar to that of lanthanum hydroxide with incorporated Si–O and Al–O complexes. Crystalline apatite structure is formed via restructuring of the polymeric structure of primary particles of amorphous lanthanum silicate during subsequent thermal treatment. Textural characteristics of produced crystalline silicates with the apatite structure are in general determined by those of amorphous precursor formed during xerogel thermal treatment in the range of 120–500 °C, which in turn results from the size and morphology of primary particle agglomerates.

Acknowledgments

This research was supported by the Russian Foundation for Basic Research, project No.14–33–50585 mol_nr, the Ministry of Education and Science of the Russian Federation and by The Tomsk State University Academic D.I. Mendeleev Fund Program grant.

Appendix A. Supporting information

Supplementary data associated with this article can be found in the online version at http://dx.doi.org/10.1016/j.ceramint.2015.07.128.

References

[1] J.C. Elliott, Structure and Chemistry of the Apatites and Other Calcium Orthophosphates, Elsevier, Amsterdam, 1994.

[2] K. Kobayashi, Y. Sakka, J. Ceram. Soc. Jpn. 122 (8) (2014) 649–663.
[3] J. Felsche, Rare earth silicates with the apatite structure, J. Solid State Chem. 5 (1972) 266–275.
[4] L.W. Schroeder, M. Mathew, Cation ordering in $Ca_2La_8(SiO_4)6O_2$, J. Solid State Chem. 26 (1978) 383–387.
[5] J. Felsche, The crystal chemistry of the rare-earth silicates, Rare Earth, Structure and Bonding, 13, Springer, Berlin, Heidelberg, 1973, p. 99–197.
[6] I.A. Bondar, N.A. Toropov, Preparation and properties of rare-earth silicates and aluminates, Mater. Res. Bull. 2 (1967) 479–489.
[7] N.A. Toropov, I. A Bondar, A.N. Lazarev, Yu. I. Smolin, Silicates of rare-earth elements and their analogues, Nauka, Leningrad, 1971.
[8] C.-H. Hsu, S. Das, Ch.-H Lu, Color-tunable, single phased $MgY_4Si_3O_{13}$: Ce^{3+}, Mn^{2+} phosphors with efficient energy transfer for white-light-emitting diodes, J. Electrochem. Soc. 159 (5) (2012) J193–J199.
[9] Ch. Peng, M. Shang, G. Li, Z. Hou, D. Geng, J. Lin, Electrospinning synthesis and luminescence properties of one-dimensional $La_{9.33}(SiO_4)6O_2$: Ln^{3+} (Ln=Ce, Eu, Tb) microfibers, Dalton Trans. 41 (2012) 4780–4788.
[10] A.M. Karpov, M.G. Zuev, Sol–gel synthesis and spectral characteristics of crystal phosphors $Sr_2Y_{8(1-x)}Eu_{8x}Si_6O_{26}$, Glass Phys. Chem. 38 (4) (2012) 431–436.
[11] N. Li, B. Zhou, S. Li, J. Zhoun, Y. Sun, Characterization and photoluminescent properties of sol-gel-derived $Ca_{2(1-x)}La_{7.6}+x(SiO_4)6O_2$:$Eu_{0.4}$, Li_x phosphors, Ceram. Int. 39 (2013) 9343–9349.
[12] Y Liu, Z. Wang, J. Zhong, F. Pan, H. Liang, Z. Xia, Synthesis and photoluminescence properties of red-emitting phosphors $Ba_2Gd_8(SiO_4)6O_2$:Eu^{3+}, Mater. Lett. 129 (2014) 130–133.
[13] J. Sokolnicki, E. Zych, Synthesis and spectroscopic investigations of $Sr_2Y_8(SiO_4)6O_2$:Eu^{2+}, Eu^{3+} phosphor for white LEDs, J. Lumin. 158 (2015) 65–69.
[14] H. Liu, Y. Zhang, L. Liao, Z. Xia, Synthesis, structure and green luminescence evolution of apatite-type $Sr_{3.5}Y_{6.5}O_2(PO_4)_{1.5}(SiO_4)_{4.5}$: Eu^{2+}, Tb^{3+} phosphors, J. Lumin. 156 (2014) 49–54.
[15] S. Nakayama, H. Aono, Y. Sadaoka, Ionic conductivity of $Ln_{10}(SiO_4)6O_3$ (Ln=La, Nd, Sm, Gd and Dy), Chem. Lett. 6 (1995) 431–432.
[16] S. Nakayama, M. Sakamoto, Electrical properties of new type high oxide ionic conductor $RE_{10}Si_6O_{27}$ (RE=La, Pr, Nd, Sm, Gd, Dy), J. Eur. Ceram. Soc. 18 (1998) 1413–1418.
[17] K. Kobayashi, Y. Sakka, Research progress in nondoped lanthanoid silicate oxyapatites as new oxygen-ion conductors, J. Ceram. Soc. Jpn. 122 (11) (2014) 921–939.
[18] E. Kendrick, M.S. Islam, P.R Slater, Developing apatites for solid oxide fuel cells: insight into structural, transport and doping properties, J. Mater. Chem. 17 (2007) 3104–3111.
[19] J.E.H. Sansom, D. Richings, P.R. Slater, A powder neutron diffraction study of the oxide-ion-conducting apatite-type phases, $La_{9.33}Si_6O_{26}$ and $La_8Sr_2Si_6O_{26}$, Solid State Ion. 139 (2001) 205–210.
[20] J.R. Tolchard, P.R. Slater, A high temperature powder neutron diffraction structural study of the apatite-type oxide ion conductor, $La_{9.67}Si_6O_{26.5}$, J. Phys. Chem. Solids 69 (2008) 2433–2439.
[21] L. Leon-Reina, E.R. Losilla, M. Martinez-Lara, S. Bruque, M.A. G. Aranda, Interstitial oxygen conduction in lanthanum oxy-apatite electrolytes, J. Mater. Chem. 14 (2004) 1142–1149.
[22] L. Leon-Reina, E.R. Losilla, M. Martinez-Lara, S. Bruque, A. Llobet D.V. Sheptyakovc, M.A.G. Aranda, Interstitial oxygen in oxygen-stoichiometric apatites, J. Mater. Chem. 15 (2005) 2489–2498.
[23] L. Leon-Reina, J.M. Porras-Vazquez, E.R. Losilla, M.A.G. Aranda, Interstitial oxide positions in oxygen-excess oxy-apatites, Solid State Ion. 177 (2006) 1307–1315.
[24] A.L. Shaula, V.V. Kharton, F.M.B. Marques, Oxygen ionic and electronic transport in apatite-type $La_{10-x}(Si,Al)_6O_{26}\pm d$, J. Solid State Chem. 178 (2005) 2050–2061.
[25] F.M.B. Marques, V.V. Kharton, E.N. Naumovich, A.L. Shaula A.V. Kovalevsky, A.A. Yaremchenko, Oxygen ion conductors for fuel cells and membranes: selected developments, Solid State Ion. 177 (2006) 1697–1703.
[26] A.L. Shaula, V.V. Kharton, J.C. Waerenborgh, D.P. Rojas, F.M. B. Marques, Oxygen ionic and electronic transport in apatite ceramics, J. Eur. Ceram. Soc. 25 (2005) 2583–2586.
[27] H. Yoshioka, Oxide ionic conductivity of apatite-type lanthanum silicates, J. Alloy. Compd. 408–412 (2006) 649–652.
[28] S. Kato, T. Yoshizawa, N. Kakuta, S. Akiyama, M. Ogasawara, T. Wakabayashi, Y. Nakahara, S. Nakata, Preparation of apatite-type-silicate-supported precious metal catalysts for selective catalytic reduction of No_x, Res. Chem. Intermed. 34 (2008) 703–708.
[29] T. Wakabayashi, S. Kato, Y. Nakahara, M. Ogasawara, S. Nakata, Oxidation property of $Pt/La_{7.33}BaYSi_6O_{25.5}$ catalysts for hydrocarbon species, Catal. Today 164 (2011) 575–579.
[30] A. Ono, M. Abe, S. Kato, M. Ogasawara, T. Wakabayashi, Y. Nakahara, S. Nakata, NO reduction property of apatite-type $La_8A_2Si_6O_{26}$ (A=Ca, Sr, Ba) supported Pt catalyst, Appl. Catal. B 103 (2011) 149–153.
[31] A. Ono, S. Kato, T. Narumi, Y. Adachi, M. Ogasawara, T. Wakabayashi, Y. Nakahara, S. Nakata, Preparation and NO reduction property of apatite-type $ALa_9Si_6O_{26}$ (A=Li, Na, K) supported Pt catalyst, J. Ceram. Soc. Jpn. 121 (2013) 169–175.
[32] X.H. Zhang, X Yi, J. Zhang, Z. Xie, J. Kang, L. Zheng, Fabrication of apatite-type $La_{9.33}(SiO_4)6O_2$ hollow nanospheres as potential energy-saving oxidative catalysts, Inorg. Chem. 49 (2010) 10244–10246.
[33] T.S. Kharlamova, A.S. Matveev, A.B. Ishchenko, A.N. Salanov S.V. Koshcheev, A.I. Boronin, V.A. Sadykov, Synthesis and physico-chemical and catalytic properties of apatite-type lanthanum silicates, Kinet. Catal. 55 (2014) 361–371.
[34] B. Li, W. Liu, W. Pan, Synthesis and electrical properties of apatite-type $La_{10}Si_6O_{27}$, J. Power Sources 195 (2010) 2196–2201.
[35] T. Yang, H. Zhao, J. Han, N. Xu, Y. Shen, Z. Du, J. Wang, Synthesis and densification of lanthanum silicate apatite electrolyte for intermediate temperature solid oxide fuel cell via co-precipitation method, J. Eur. Ceram. Soc. 34 (2014) 1563–1569.
[36] H. Li, T. Baikie, S.S. Pramana, J.F. Shin, P.J. Keenan, P.R. Slater, F. Brink, J. Hester, T. An, T.J. White, Hydrothermal synthesis, structure investigation, and oxide ion conductivity of mixed Si-Ge-based apatite-type phases, Inorg. Chem. 53 (10) (2014) 4803–4812.
[37] S.W. Tao, J.T.S. Irvine, Synthesis and ionic conduction of apatite-type materials, Ionics 6 (2000) 389–396.
[38] S. Tao, J.T.S. Irvine, Preparation and characterisation of apatite-type lanthanum silicates by a sol–gel process, Mater. Res. Bull. 36 (2001) 1245–1258.
[39] S. Celerier, C. Laberty, F. Ansart, P. Lenormand, P. Stevens, New chemical route based on sol–gel process for the synthesis of oxyapatite $La_{9.33}Si_6O_{26}$, Ceram. Int. 32 (2006) 271–276.
[40] S. Celerier, C. Laberty-Robert, F. Ansart, C. Calmet, P. Stevens, Synthesis by sol–gel route of oxyapatite powders for dense ceramics: applications as electrolytes for solid oxide fuel cells, J. Eur. Ceram. Soc. 25 (2005) 2665–2668.
[41] Y. Masubuchi, M. Higuchi, T. Takeda, S. Kikkawa, Preparation of apatite-type $La_{9.33}(SiO_4)6O_2$ oxide ion conductor by alkoxide-hydrolysis, J. Alloy. Compd. 408–412 (2006) 641–644.
[42] K. Kobayashi, T.S. Suzuki, T. Uchikoshi, Y. Sakka, Low-temperature formation of Ln silicate oxyapatite (Ln=La and Nd) by the water-based sol–gel method, Solid State Ion. 204–205 (2011) 91–96.
[43] E. Jothinathan, K. Vanmeensel, J. Vleugels, O. Van der Biest, Powder synthesis, processing and characterization of lanthanum silicates for SOFC application, J. Alloy. Compd. 495 (2010) 552–555.
[44] C. Tian, J. Liu, J. Cai, Y. Zeng, Direct synthesis of $La_{9.33}Si_6O_{26}$ ultrafine powder via sol–gel self-combustion method, J. Alloy. Compd. 458 (2008) 378–382.
[45] Q. Shi, L. Lu, Y. Zeng, H. Zhang, Influence of pH on the Property of apatite-type lanthanum silicates prepared by sol–gel process, J. Wuhan Univ. Technol.-Mater. Sci. Ed. 27 (2012) 841–846.
[46] E. Rodriguez-Reyna, A.F. Fuentes, M. Maczka, J. Hanuza, K. Boulahya, U. Amador, Structural, microstructural and vibrational characterization of apatite-type lanthanum silicates prepared by mechanical milling, J. Solid State Chem. 179 (2006) 522–531.
[47] A.F. Fuentes, E. Rodriguez-Reyna, L.G. Martinez-Gonzalez, M. Maczka, J. Hanuza, U. Amador, Room-temperature synthesis of apatite-type lanthanum silicates by mechanically milling constituent oxides, Solid State Ion. 177 (2006) 1869–1873.

[48] T. Kharlamova, S. Pavlova, V. Sadykov, M. Chaikina, T. Krieger, O. Lapina, D. Khabibulin, A. Ishchenko, V. Zaikovskii, Chr. Argirusis, J. Frade, Al-doped apatite-type nanocrystalline lanthanum silicates prepared by mechanochemical synthesis: phase, structural and microstructural study, Eur. J. Inorg. Chem. 6 (2008) 939–947.
[49] T. Kharlamova, S. Pavlova, V. Sadykov, M. Chaikina, T. Krieger, A. Ishchenko, Y. Pavlyukhin, S. Petrov, Chr. Argirusis, Mechanochemical synthesis of Fe-doped apatite-type lanthanum silicates, Eur. J. Inorg. Chem. 4 (2010) 589–601.
[50] V.A. Dzisko, A.P. Karnaukhov, D.V. Tarasova, Physico-Chemical Foundations of Oxide Catalyst Synthesis, Nauka, Novosibirsk, 1978.
[51] M. Campanati, G. Fornasari, A. Vaccari, Fundamentals in the preparation of heterogeneous catalysts, Catal. Today 77 (2003) 299–314.
[52] R.A. Buyanov, O.P. Krivoruchko, Preparation of oxide catalysts: from the studies of the mechanisms of synthesis and crystallization towards control of properties, React. Kinet. Catal. Lett. 35 (1987) 293–302.
[53] M. Kakihana, "Sol–gel" preparation of high temperature superconducting oxides, J. Sol-Gel Sci. Technol. 6 (1996) 7–55.
[54] M. Salavati-Niasari, G. Hosseinzadeh, F. Davar, Synthesis of lanthanum carbonate nanoparticles via sonochemical method for preparation of lanthanum hydroxide and lanthanum oxide nanoparticles, J. Alloy. Compd. 509 (2011) 134–140.
[55] R.P. Turcotte, J.O. Sawyer, L. Eyring, On the rare earth dioxymonocarbonates and their decomposition, Inorg. Chem. 8 (1969) 238–246.
[56] B. Klingenberg, M.A. Vannice, Influence of pretreatment on lanthanum nitrate, carbonate, and oxide powders, Chem. Mater. 8 (1996) 2755–2768.
[57] A.N. Lazarev, A.P. Mirgorodsky, I.S. Ignatyev, Vibration Spectra of Complex Oxides. Silicates and Their Analogues, Nauka, Leningrad, 1975.
[58] I.I. Plyusnina, Infrared Spectra of Silicates, Moscow University, Moscow, 1967.
[59] R. Dupree, M.H. Lewis, M.E. Smith, A high-resolution NMR study of the La–Si–A1–O–N system, J. Am. Chem. Soc. 111 (1989) 5125–5132.
[60] D. Freude, J. Kärger, NMR techniques, in: F. Schüth, K.S.W. Sing, J. Weitkamp (Eds.), Handbook of Porous Solids, 1, Wiley-VCH, Weinheim, 2002, pp. 465–504.
[61] D. Iuga, S. Simon, E. de Boer, A.P.M. Kentgens, A nuclear magnetic resonance study of amorphous and crystalline lanthanum-aluminates, J. Phys. Chem. B 103 (1999) 7591–7598.
[64] R. Boistelle, J.P. Astier, Crystallization mechanisms in solution, J. Cryst. Growth 90 (1988) 14–30.
[65] A.A. Chernov, Formation of crystals in solutions, Contemp. Phys. 30 (4) (1989) 251–276.
[66] A.I. Moshinskii, Stability analysis of the growth of particles of a polydisperse system in a solution under nonisothermal conditions, J. Appl. Mech. Tech. Phys. 41 (6) (2000) 1044–1053.
[67] A. Bernardo, M Giulietti, Modeling of crystal growth and nucleation rates for pentaerythritol batch crystallization, Chem. Eng. Res. Des. 88 (2010) 1356.
[68] O.D. Linnikov, Mechanism of precipitate formation during spontaneous crystallization from supersaturated aqueous solutions, Russ. Chem. Rev. 83 (4) (2014) 343–364.
[69] O.P. Krivoruchko, R.A. Buyanov, B.P. Zolotovskii, A.A. Ostan'kovich, Investigation of the properties of primary polymer particles of freshly precipitated Fe^{3+} hydrogels, Russ. Chem. Bull. 23 (7) (1974) 1384–1389.
[70] O.P. Krivoruchko, B.P. Zolotovskii, L.M. Plyasova, R.A. Buyanov V.I. Zaikovskii, Boehmite formation mechanism in precipitate ageing, React. Kinet. Catal. Lett. 21 (1–2) (1982) 103–108.
[71] O.P. Krivoruchko, R.A. Buyanov, B.P. Zolotovskii, Izv. SOAN SSSR, Ser. Khim. Nauk 2 (1980) 26–29.
[72] V.I. Kuznetsov, E.N. Yurchenko, M.T. Protasova, E.A. Taraban O.P. Krivoruchko, R.A. Buyanov, Mossbauer investigation of the influence of Al (III) ions on the properties of mixed Fe (III)-Bl(III) hydroxides and oxides, Phys. Status Solidi 113 (1989) 359–364.
[73] E.A. Taraban, V.I. Zaikovskii, O.P. Krivoruchko, The unusual morphological structure of the aging products of coprecipitated Fe(III)–Al(III) hydroxides, Russ. Chem. Bull. 39 (4) (1990) 837–838.
[74] T. Brylewski, M.M Bucko, Low-temperature synthesis of lanthanum monoaluminate powders using the co-precipitation–calcination technique, Ceram. Int. 39 (2013) 5667–5674.
[75] H. Takeda, M. Ohgaki, T. Kizuki, K. Hashimoto, Y. Toda, S. Udagawa, K. Yamashita, Formation mechanism and synthesis of apatite-type structure $Ba_{2+x}La_{8-x}(SiO_4)6O_{2-\delta}$, J. Am. Ceram. Soc. 83 (2000) 2884–2886.
[76] L. Zhang, H. Q He., H. Wu, C.-Z. Li, S.P. Jiang, Synthesis and characterization of doped $La_9ASi_6O_{26.5}$ (A=Ca, Sr, Ba) oxyapatite electrolyte by a water-based gel-casting route, Int. J. Hydrog. Energy 36 (2011) 6862–6874.
[77] S.P. Jiang, L. Zhang, H.Q. He, R.K. Yap, Y. Xiang, Synthesis and characterization of lanthanum silicate apatite by gel-casting route as electrolytes for solid oxide fuel cells, J. Power Sources 189 (2009) 972–981.
[78] E. Janots, F. Brunet, B. Goffe, Ch. Poinssot, M. Burchard, L. Cemic, Thermochemical characterization of $Ca_4La_6(SiO_4)6(OH)_2$ a synthetic La- and OH-analogous of britholite: implication for monazite and LREE apatites stability, Mineralogia 39 (1–2) (2008) 41–52.
[79] M. Ozawa, R. Onoe, H. Kato, Formation and decomposition of some rare earth (RE=La, Ce, Pr) hydroxides and oxides by homogeneous precipitation, J. Alloy. Compd. 408–412 (2006) 556–559.
[80] G. Li, C. Li, Z. Xu, Z. Cheng, J. Lin, Facile synthesis, growth mechanism and luminescence properties of uniform $La(OH)_3$: Ho^{3+}/Yb^{3+} and La_2O_3: Ho^{3+}/Yb^{3+} nanorods, CrystEngComm 12 (2010) 4208–4216.
[81] S. Bernal, G. Blanco, J.M. Gatica, J.A. Perez-Omil, J.M. Pintado, H. Vidal, Chemical reactivity of binary rare earth oxides: in, in: G. Adachi et al.(Ed.), Springer, Netherlands, XIV, 2004, pp. 9–55.
[82] N.V. Belov, Structural analysis and crystal chemistry of silicates in USSR, Kristallografiya 12 (5) (1967) 775–785.
[83] N.V. Belov, A second chapter in the chemical crystallography of the silicates, J. Struct. Chem. 1 (1) (1960) 35–43.